

THE SURVEY FOR IONIZATION IN NEUTRAL GAS GALAXIES- II. THE STAR FORMATION RATE DENSITY OF THE LOCAL UNIVERSE

D.J. HANISH¹, G.R. MEURER¹, H.C. FERGUSON², M.A. ZWAAN³, T.M. HECKMAN¹, L. STAVELEY-SMITH⁴, J. BLAND-HAWTHORN⁵, V.A. KILBORN^{6,4}, B.S. KORIBALSKI⁴, M.E. PUTMAN⁷, E.V. RYAN-WEBER⁸, M.S. OEY⁷, R.C. KENNICUTT, JR.⁹, P.M. KNEZEK¹⁰, M.J. MEYER³, R.C. SMITH¹¹, R.L. WEBSTER¹², M.A. DOPITA¹³, M.T. DOYLE¹⁴, M.J. DRINKWATER¹⁴, K.C. FREEMAN¹³, J.K. WERK⁷

Submitted to ApJ 2006 January 3, Accepted 2006 March 20

ABSTRACT

We derive observed H α and R band luminosity densities of an HI-selected sample of nearby galaxies using the SINGG sample to be $l'_{\text{H}\alpha} = (9.4 \pm 1.8) \times 10^{38} h_{70} \text{ erg s}^{-1} \text{ Mpc}^{-3}$ for H α and $l'_R = (4.4 \pm 0.7) \times 10^{37} h_{70} \text{ erg s}^{-1} \text{ \AA}^{-1} \text{ Mpc}^{-3}$ in the R band. This R band luminosity density is approximately 70% of that found by the Sloan Digital Sky Survey. This leads to a local star formation rate density of $\log(\dot{\rho}_{\text{SFR}} [\text{M}_{\odot} \text{ yr}^{-1} \text{ Mpc}^{-3}]) = -1.80^{+0.13}_{-0.07}(\text{random}) \pm 0.03(\text{systematic}) + \log(h_{70})$ after applying a mean internal extinction correction of 0.82 magnitudes. The gas cycling time of this sample is found to be $t_{\text{gas}} = 7.5^{+1.3}_{-2.1}$ Gyr, and the volume-averaged equivalent width of the SINGG galaxies is $EW(\text{H}\alpha) = 28.8^{+7.2}_{-4.7} \text{ \AA}$ ($21.2^{+4.2}_{-3.5} \text{ \AA}$ without internal dust correction). As with similar surveys, these results imply that $\dot{\rho}_{\text{SFR}}(z)$ decreases drastically from $z \sim 1.5$ to the present. A comparison of the dynamical masses of the SINGG galaxies evaluated at their optical limits with their stellar and HI masses shows significant evidence of downsizing: the most massive galaxies have a larger fraction of their mass locked up in stars compared with HI, while the opposite is true for less massive galaxies. We show that the application of the Kennicutt star formation law to a galaxy having the median orbital time at the optical limit of this sample results in a star formation rate decay with cosmic time similar to that given by the $\dot{\rho}_{\text{SFR}}(z)$ evolution. This implies that the $\dot{\rho}_{\text{SFR}}(z)$ evolution is primarily due to the secular evolution of galaxies, rather than interactions or mergers. This is consistent with the morphologies predominantly seen in the SINGG sample.

Subject headings: galaxies: evolution – galaxies: ISM – galaxies: starburst – stars: formation – surveys

1. INTRODUCTION

The star formation rate density of the universe has changed considerably since $z \sim 2$, decreasing by approximately an order of magnitude. This decrease has been widely discussed (e.g. Madau *et al.* 1996; Pei, Fall, & Hauser 1999; Somerville *et al.* 2001; Hopkins

2004) because the evolution of the star formation rate density acts to constrain all models of galaxy formation and evolution. Redshift-dependent luminosity densities (such as the R band luminosity density $l_R(z)$) and star formation rate densities ($\dot{\rho}_{\text{SFR}}(z)$) remain some of the best constraints on these models. The value of $l_R(z)$ at $z \approx 0$ constrains the evolution of stellar mass (Madau *et al.* 1998). Likewise, the value of $\dot{\rho}_{\text{SFR}}(z)$ at $z \approx 0$ helps determine the relative contributions of burst and quiescent star formation (Somerville *et al.* 2001) and the chemical evolution of the universe (Pei & Fall 1995). Estimates of $\dot{\rho}_{\text{SFR}}$ from previous studies span a factor of two or more, and do not always agree within their stated uncertainties, as shown in Table 1. All surveys suffer biases, however, and these may explain the large discrepancies between the densities derived from each.

The process of star formation leaves measurable signatures across the electromagnetic spectrum, allowing numerous methods for selecting star-forming galaxies, each with its own set of biases. For example, objective prism surveys for emission line galaxies (e.g. Gallego *et al.* 1995; Gronwall 1997) result in a large, consistent bias towards galaxies with high surface brightness, high equivalent width emission lines (e.g. Salzer 1989). Ultraviolet (UV) surveys (e.g. Treyer *et al.* 1998) are biased against galaxies highly attenuated by dust. Conversely, far-infrared (FIR) (e.g. Flores *et al.* 1999; Pérez-González *et al.* 2005) or sub-millimeter surveys select galaxies by the presence of dust-reprocessed optical and UV light, resulting in a bias against galaxies

¹ Department of Physics and Astronomy, The Johns Hopkins University, 3400 North Charles St., Baltimore, MD 21218-2686, hanish@pha.jhu.edu

² Space Telescope Science Institute, 3700 San Martin Drive, Baltimore, MD 21218

³ European Southern Observatory, Karl-Schwarzschild-Str. 2, D-85748 Garching b. München, Germany

⁴ Australia Telescope National Facility, CSIRO, P.O. Box 76, Epping, NSW 1710, Australia.

⁵ Anglo-Australian Observatory, P.O. Box 296, Epping, NSW 2121, Australia

⁶ Centre for Astrophysics and Supercomputing, Swinburne University of Technology, Mail 39, P.O. Box 218, Hawthorn, VIC 3122, Australia

⁷ Department of Astronomy, University of Michigan, Ann Arbor, MI 48109

⁸ Institute of Astronomy, University of Cambridge, Madingley Road, Cambridge, CB3 0HA, UK

⁹ Steward Observatory, University of Arizona, Tucson, AZ 85721

¹⁰ WIYN, Inc., 950 North Cherry Ave., Tucson, AZ 85726

¹¹ Cerro Tololo Inter-American Observatory (CTIO), Casilla 603, La Serena, Chile

¹² School of Physics, University of Melbourne, Parkville, VIC 3010, Australia

¹³ Research School of Astronomy and Astrophysics (RSAA), Australian National University, Cotter Road, Weston Creek, ACT 2611, Australia

¹⁴ Department of Physics, University of Queensland, Brisbane, QLD 4072, Australia

possessing little dust. Similarly, 1.4 GHz radio surveys (e.g. Serjeant *et al.* 2002) bias against systems with low dust content (Bell 2003); in addition, the correlation between radio flux and FIR flux (which is then used to calculate star formation rate) is not linear, resulting in a pronounced bias against low luminosity galaxies (Devereux & Eales 1989; Yun, Reddy, & Condon 2001).

The 21-cm spectral line of neutral hydrogen (HI) presents a useful starting point for star formation surveys. New stars form out of the interstellar medium, of which HI is a key component. While it is the molecular component of the ISM from which new stars form, a strong correlation has been found between HI surface density and star formation intensity (Kennicutt 1998). HI flux is unaffected by dust extinction, and has been measured in every type of star-forming galaxy. As a result, selecting targets by HI mass creates a sample set free of the common optical biases. For this, we use the HI Parkes All Sky Survey (HiPASS), an HI survey of the southern sky ($\delta \leq +2^\circ$) over a velocity range from -1280 to $+12700$ km s $^{-1}$ obtained with the 21-cm multibeam receiver (Staveley-Smith *et al.* 1996) at the 64m Parkes radio telescope (Barnes *et al.* 2001).

We have commenced the Survey of Ionization in Neutral Gas Galaxies (SINGG) to survey star formation in the HiPASS galaxies. Meurer *et al.* (2006, hereafter Paper I) introduce the SINGG survey, including sample selection, methods used, and basic measurements. In total the SINGG sample set includes 468 HI-selected targets covering the mass range $7.0 \leq \log(\mathcal{M}_{\text{HI}}/\mathcal{M}_\odot) \leq 11.0$ in approximately equal numbers per decade of mass. Distance was also used in the selection process; the nearest sources were preferentially selected at each mass to improve physical resolution and avoid confusion.

To measure star formation, SINGG uses H α , the most readily accessible optical tracer of star formation at low redshifts. H α is a recombination line primarily resulting from hydrogen photoionization. Because this requires ionizing UV photons, the majority of H α flux will be produced near the most massive O stars, whose extremely short lifespans ($\lesssim 10$ Myr) make them good indicators of the current star formation rate. SINGG uses R band measurements for continuum subtraction, which also provide useful measurements of the existing stellar populations. Observations presented in Paper I consist of the 93 HiPASS extragalactic HI targets fully processed to date. Due to the large beam size of HiPASS, 13 of these HI targets contain between two and four distinct H α objects. As a result, the SINGG sample includes a total of 111 individual H α -emitting galaxies, which we refer to as SINGG Release 1, or SR1. We however exclude one HI target, J0403-01, and its single H α -emitting galaxy due to excessive sky uncertainties and foreground field contamination. The results included in this paper are entirely generated from the data presented in Paper I.

This paper uses the SINGG observations to derive the H α and R band luminosity densities of the local universe, designated $l_{\text{H}\alpha}(z)$ and $l_R(z)$ respectively, where z indicates the mean redshift of the survey. For this and most of the other local ($z \approx 0$) studies, we will omit the (z) notation except where required. Combined with the HI data from HiPASS, these yield the star formation rate density of the local universe, the stellar luminosity

density, the density of the neutral ISM, and the cosmic gas cycling time. Section 2 explains the methodology used to determine the various volume densities and their uncertainties. Section 3 gives the results of our calculations. Section 4 gives the results and compares to those of other surveys, while Section 5 discusses some of the implications of our results. We use a Λ CDM cosmology ($\Omega_0 = 0.3$, $\Omega_\Lambda = 0.7$) with a Hubble constant of $H_0 = 70$ km s $^{-1}$ Mpc $^{-1}$, and a Salpeter (1955) IMF between 0.1 and 100 \mathcal{M}_\odot .

2. METHODOLOGY

2.1. HI mass

Since the SINGG sample is not volume complete, we tie our results to an HI Mass Function (HiMF). HI parameters are primarily derived from the data given in our two main source catalogs: HiCAT, the final HiPASS catalog (Meyer *et al.* 2004), and BGC, the HiPASS Bright Galaxy Catalog (Koribalski *et al.* 2004). These catalogs have 95% completeness limits in velocity-integrated 21 cm flux densities of $\int S_\nu dv \sim 5$ and 25 Jy km s $^{-1}$, respectively. The HI mass of a galaxy at a distance of D Mpc is derived using the standard relation $\mathcal{M}_{\text{HI}} [\mathcal{M}_\odot] = 2.36 \times 10^5 D^2 \int S_\nu dv [\text{Jy km s}^{-1}]$ (Roberts 1962). As a result, the flux density limits for these two samples correspond to HI mass limits of 1.2 and $5.9 \times 10^6 D^2 \mathcal{M}_\odot$, respectively. The SR1 sources have distances of 4 – 73 Mpc (with the majority falling within the 10 – 20 Mpc range) and HI masses of $10^{7.5} - 10^{10.6} \mathcal{M}_\odot$. Detailed information about the HI masses of the SINGG galaxies can be found in the original catalog publications and Paper I.

Distances for most sources are derived from radial velocities using the model of Mould *et al.* (2000), which corrects for infalls towards the Virgo cluster, Great Attractor, and Shapley supercluster. Distances to the nearest galaxies are taken from Karachentsev *et al.* (2004). This alters the distances and HI masses for many SINGG galaxies when compared to other HiPASS papers (Zwaan *et al.* 2005), and marginally alters the HI Mass Function used to correct for incompleteness. The values given throughout this paper are those derived using the Mould model for the full HiPASS sample.

We use the standard Schechter function to parameterize the HiMF:

$$\theta(\mathcal{M}_{\text{HI}}) d\mathcal{M}_{\text{HI}} = \theta_* \left(\frac{\mathcal{M}_{\text{HI}}}{\mathcal{M}_*} \right)^\alpha e^{-\left(\frac{\mathcal{M}_{\text{HI}}}{\mathcal{M}_*} \right)} d\left(\frac{\mathcal{M}_{\text{HI}}}{\mathcal{M}_*} \right) \quad (1)$$

where $\theta(\mathcal{M}_{\text{HI}})$ represents the number density of galaxies as a function of HI mass (in Mpc $^{-3}$), \mathcal{M}_* is the characteristic mass, α is the “faint” end slope and θ_* is the normalization factor. We calculate Schechter fits to raw, binned $\theta(\mathcal{M}_{\text{HI}})$ data from Zwaan *et al.* (2005), and adjusted to the distance of Mould *et al.* (2000) for $H_0 = 70$ km s $^{-1}$ Mpc $^{-1}$. This yields $\mathcal{M}_* = 10^{9.92 \pm 0.04} h_{70}^{-2} \mathcal{M}_\odot$, $\alpha = -1.41 \pm 0.05$ and $\theta_* = (3.86 \pm 0.7) \times 10^{-3} h_{70}^3 \text{Mpc}^{-3} \text{dex}^{-1}$; these values are compared to other HI Mass Functions in Table 2. As is usually the case, the errors on \mathcal{M}_* and θ_* are highly correlated.

For the 13 SR1 HI targets containing multiple H α sources, HiPASS can only provide the total HI mass for each target, with no ability to distinguish the contributions of each individual galaxy. When calculating

our luminosity densities, the luminosities of the individual galaxies within each HI target are combined and the total is treated as a single aggregate object. As the mass function given above was generated using similarly combined HI masses, this approach should not substantially bias our results.

2.2. Volume densities

Using the HiMF, we derive the R continuum luminosity density l_R , $H\alpha$ luminosity density $l_{H\alpha}$, and HI mass density ρ_{HI} for the local universe. We denote values uncorrected for internal extinction with a prime (') symbol.

The volume density of a quantity x is found using:

$$n_x = \int \theta(\mathcal{M}_{HI}) x(\mathcal{M}_{HI}) d\left(\frac{\mathcal{M}_{HI}}{\mathcal{M}_*}\right) \quad (2)$$

where $x = L_{H\alpha}$ when calculating $l_{H\alpha}$, $x = L_R$ when calculating l_R , $x = 1.0$ when calculating the number density n , or $x = \mathcal{M}_{HI}$ when calculating ρ_{HI} .

By separating our data into HI mass bins and combining the results within each bin, Eq. 2 is replaced by:

$$n_x = \ln(10) \sum_{i=1}^{N_{bins}} \frac{\Delta \log(\mathcal{M}_{HI})_i}{N_i} \sum_{j=1}^{N_i} \theta(\mathcal{M}_{HIj}) x_j \left(\frac{\mathcal{M}_{HIj}}{\mathcal{M}_*} \right) \quad (3)$$

Here, i represents the array of mass bins, while j represents the individual HiPASS targets within each bin. $\Delta \log(\mathcal{M}_{HI})_i$ is the logarithmic width of each mass bin; our bins are 0.5 decades wide for all bins except the lowest ($7.0 \leq \log(\mathcal{M}_{HI}/\mathcal{M}_\odot) \leq 8.0$), as shown in Table 3.

The SR1 $H\alpha$ and R luminosities are given in Paper I, along with lists of targets containing multiple emission line galaxies. These luminosities are derived from fluxes extracted using elliptical apertures, supplemented with the flux from outer disk HII regions. Full discussions of our R and $H\alpha$ flux extraction procedures are given in Paper I.

To calculate the Star Formation Rate (SFR) for each galaxy, we adopt the conversion from $H\alpha$ luminosity to SFR given by Kennicutt *et al.* (1994). This relationship is derived using a single power law Initial Mass Function (IMF) having a Salpeter (1955) slope and spanning the mass range of 0.1 to $100 \mathcal{M}_\odot$. The resulting conversion is

$$SFR [\mathcal{M}_\odot \text{ yr}^{-1}] = \left(\frac{L_{H\alpha} [\text{erg s}^{-1}]}{1.26 \times 10^{41}} \right) \quad (4)$$

We adopt this conversion to maintain consistency with numerous other studies. The choice in IMF is a major source of systematic uncertainty, since the conversion of $L_{H\alpha}$ to SFR depends entirely on the fraction of stars falling within the mass range responsible for ionizing hydrogen. For example, the various IMFs of Scalo (1986) would decrease the conversion factor to anywhere from 1.7×10^{40} to 8.4×10^{40} (Kennicutt *et al.* 1994), and that of Kroupa (2001) would give a conversion of 1.9×10^{41} (Brinchmann *et al.* 2004). However, all $H\alpha$ surveys suffer from this bias equally, and so as with H_0 , we convert other $H\alpha$ surveys to our chosen IMF before comparison.

2.3. Flux corrections

To calculate star formation rates, we first have to correct the flux data for foreground and internal extinction, [NII] contamination, and stellar absorption. The

foreground extinction corrections are accomplished using the Schlegel, Finkbeiner & Davis (1998) extinction maps. Since our selection avoids the Galactic plane and the Magellanic clouds, the foreground extinction correction increases the derived values of $l_{H\alpha}$ and l_R by an average of only 10%. Stellar absorption, as explained in Paper I, causes our measurements to consistently underestimate $H\alpha$ flux by 2 – 6% (Brinchmann *et al.* 2004). To adjust for this, we increase each of our $H\alpha$ fluxes by 4%.

For the [NII] correction and internal dust absorption, $A(H\alpha)_{int}$, we adopt the relationships with R band absolute magnitude prior to dust absorption corrections, M'_R , given by Helmboldt *et al.* (2004) and converted to the AB magnitude system, as explained in Paper I. Each galaxy's individual [NII]/ $H\alpha$ correction is based on its HI velocity, velocity width, and the narrow-band transmission profile, as detailed in Paper I. Integrated over our entire sample, the [NII] correction decreases $l_{H\alpha}$ by 15%; l_R is not affected. The internal extinction correction $A(H\alpha)_{int}$ increases our estimate of $l_{H\alpha}$ by a factor of 2.1 (0.82 mag). As noted in Paper I, we assume that the R band internal dust absorption, $A(R)_{int}$, is half that of $A(H\alpha)_{int}$, due to the well-known phenomenon of increased extinction in HII regions compared to the field (Fanelli, O'Connell, & Thuan 1988; Calzetti, Kinney & Storchi-Bergman 1994), and so l_R increases by 0.41 magnitudes after extinction correction.

3. RESULTS

3.1. Volume densities

The R band luminosity density, corrected only for Galactic extinction, is found to be

$$l'_R = (4.4 \pm 0.7) \times 10^{37} h_{70} \text{ erg s}^{-1} \text{ \AA}^{-1} \text{ Mpc}^{-3} \quad (5)$$

while the $H\alpha$ luminosity density, corrected for [NII] contamination and Galactic extinction, is

$$l'_{H\alpha} = (9.4 \pm 1.8) \times 10^{38} h_{70} \text{ erg s}^{-1} \text{ Mpc}^{-3}. \quad (6)$$

With our adopted IMF and resultant star formation rate conversion, Eq. 4, the local star formation rate density (uncorrected for internal extinction) is

$$\log(\dot{\rho}'_{SFR} [\mathcal{M}_\odot \text{ yr}^{-1} \text{ Mpc}^{-3}]) = -2.13^{+0.08}_{-0.09}(\text{ran.}) \pm 0.03(\text{sys.}) + \log(h_{70}) \quad (7)$$

Corrected for internal dust extinction, these equations become:

$$l_R = 7.0^{+1.5}_{-0.3} \times 10^{37} h_{70} \text{ erg s}^{-1} \text{ \AA}^{-1} \text{ Mpc}^{-3} \quad (8)$$

$$l_{H\alpha} = 2.0^{+0.6}_{-0.4} \times 10^{39} h_{70} \text{ erg s}^{-1} \text{ Mpc}^{-3} \quad (9)$$

$$\log(\dot{\rho}_{SFR} [\mathcal{M}_\odot \text{ yr}^{-1} \text{ Mpc}^{-3}]) = -1.80^{+0.13}_{-0.07}(\text{ran.}) \pm 0.03(\text{sys.}) + \log(h_{70}) \quad (10)$$

The uncertainties in each variable are explained in detail in subsections 3.2 and 3.3.

Additionally, we derive the HI mass density to be

$$\rho_{HI} = 5.17 \pm 0.38 \times 10^7 h_{70} \mathcal{M}_\odot \text{ Mpc}^{-3} \quad (11)$$

and the mean number density of HI-rich galaxies to be

$$n = 0.112^{+0.017}_{-0.024} h_{70} \text{ Mpc}^{-3} \quad (12)$$

within our mass range, $7.0 \leq \log(\mathcal{M}_{\text{HI}}/\mathcal{M}_{\odot}) \leq 11.0$. Unlike the luminosity densities, this number density is completely dependent on the lower boundary chosen, as the integrated function increases as \mathcal{M}_{HI} decreases. Fig. 1 shows the dependence of the luminosity densities (and, by extension, derived quantities such as $\dot{\rho}_{\text{SFR}}$) on \mathcal{M}_{HI} , along with the systematic uncertainty in the total value due to each bin. The plotted quantity is the fraction of the total luminosity density coming from one decade of mass.

For comparison, we also derive $\dot{\rho}_{\text{SFR}}$ and ρ_{HI} for other mass functions, using the simpler distance model favored by HiPASS; these values are given in Table 2. Only the HiMF weighting of each $\text{H}\alpha$ source is altered; the distances and fluxes remain unchanged. While the differences in individual HiMF parameters are relatively small, the resulting integrated mass and luminosity densities in Table 2 vary by 0.20 – 0.22 dex, primarily due to the low-mass slope, α . While this discrepancy is comparable to the total uncertainties in each density, it is significantly larger than the ~ 0.03 dex uncertainty caused by the uncertainties in the HiMF parameters themselves.

3.2. Random errors

Since the calculations of luminosity densities involve many different variables, most of which have their own uncertainties, the simple methods of error propagation would result in heavily correlated uncertainties. To better quantify the random uncertainties, we utilize Monte Carlo and “bootstrap” algorithms.

We consider the following sources of random error: (1) the HiMF: the limited number of HiPASS sources used to derive each HiMF results in uncertainties in the parameters used to fit that HiMF, and hence on luminosity densities; (2) error due to the limited SINGG SR1 sample; (3) R and $\text{H}\alpha$ flux uncertainties due to sky subtraction; (4) $\text{H}\alpha$ flux uncertainty due to continuum subtraction; (5) the uncertainty in the $\text{H}\alpha$ flux calibration, and (6-7) error due to the dispersion in the fits used to generate our [NII] and $A(\text{H}\alpha)_{\text{int}}$ corrections. The random errors are presented in Table 4; we consider each of these terms in detail.

To estimate the uncertainty due to the HiMF, we create one hundred realizations of the HiMF using a bootstrap resampling of the original data in HiCAT and adopting the Mould *et al.* (2000) distance model. The HiMF in each realization is created using the same two dimensional stepwise maximum likelihood technique of Zwaan *et al.* (2005). Each realized HiMF is fit to a Schechter function, which is used in Eq. 3 to determine the resulting luminosity densities of each realization. The random uncertainty in each luminosity density due to the HiMF is then the dispersion about the mean luminosity density for all the realizations.

To quantify the SR1 sampling error we use a “bootstrap” resampling method, drawing 92 objects at random (with duplication allowed) from our data set. As with our other uncertainties, this randomization is repeated ten thousand times, with the overall sampling uncertainty defined as the standard deviation of the resulting distribution.

The errors due to the uncertainties in the continuum scaling ratio and background sky level for each galaxy are quantified through another form of Monte Carlo logic.

For each of ten thousand iterations, we vary the sky level or continuum ratio within Gaussian distributions having the uncertainties derived from our error models, which in turn alter the measured flux (and by extension, the star formation rate) for each galaxy. Again, the luminosity densities are recalculated for each iteration, and the dispersion about the mean is quoted as the resulting uncertainty. Additionally, we have an uncertainty due to our flux calibration method, as explained in Paper I; we estimate this uncertainty to be 0.04 magnitudes for images requiring our 6568/28 narrow-band filter, and 0.02 magnitudes for all others.

To find the random error due to our $A(\text{H}\alpha)_{\text{int}}$ and [NII] corrections, we use the M'_R fits given in Helmboldt *et al.* (2004), each of which has a dispersion of 0.23 dex (Helmboldt, priv. comm.). We make a series of realizations of our sample; within each realization, each galaxy’s $\log(A(\text{H}\alpha)_{\text{int}})$ or $\log(F_{[\text{NII}]6583}/F_{\text{H}\alpha})$ correction is perturbed by a Gaussian random deviate with the above dispersion. Luminosity densities are re-derived, and the dispersion about the mean simulated luminosity density is our random error. Separate sets of realizations are done to determine the errors due to $A(\text{H}\alpha)_{\text{int}}$ and those due to the [NII] correction, with all other terms held fixed.

Applied to the SINGG sample, we find the uncertainties as listed in Table 4. We find that the random uncertainties are dominated by the internal dust extinction (for the corrected luminosity densities only), the SR1 sampling error, and to a lesser extent the HiMF uncertainties. While the sky and continuum subtraction uncertainties dominate the measurements of many individual galaxies, when evaluated over our entire sample their contributions to the error budget are relatively small.

3.3. Systematic errors

The SINGG results also suffer from a series of systematic uncertainties. We consider the following sources of systematic error: (1 – 2) uncertainty in the zeropoints of our [NII] and $A(\text{H}\alpha)_{\text{int}}$ corrections; (3) variation due to our choice of distance model; (4) variation due to our choice of HiMF.

In addition to the dispersion mentioned in Section 3.2, our $A(\text{H}\alpha)_{\text{int}}$ and [NII] corrections include an uncertainty in the fit from Helmboldt *et al.* (2004) itself. This zero-point uncertainty corresponds to the discrepancy in luminosity density for fits one standard deviation of mean away from the best fit, generated from the 196 sources of Jansen (2000).

Our distance model is a significant source of systematic uncertainty, as most SINGG targets are located within a distance of 20 Mpc. Variations in the distances used can result in large changes in observed luminosities as well as the underlying HI Mass Function, and as a result alter the derived star formation rates. To quantify this effect, we calculate $\dot{\rho}_{\text{SFR}}$ using both our default Mould *et al.* (2000) distance model as well as the simpler local-group model used by Zwaan *et al.* (2005), and quote the difference as our uncertainty.

Finally, we calculate our luminosity densities using a variety of HI mass functions and the local-group distance model, with results shown in Table 2. While the HiPASS team has produced several HI mass functions, each supersedes the one before, with the work of Zwaan *et al.*

(2005) comprising the most complete version. As a result, while the resulting values of $\dot{\rho}_{\text{SFR}}$ vary by non-negligible amounts, the earlier H1MF values are only for comparison purposes, and we do not include this error in our final uncertainties.

Our quoted systematic uncertainties are completely dominated by our choice of distance model.

3.4. Equivalent width

We define the volume-averaged H α equivalent width to be the ratio of H α flux density to R band flux density. We find the volume-averaged equivalent width of our sample to be

$$EW'(\text{H}\alpha) = 21.2^{+4.2}_{-3.5} \text{ \AA} \quad (13)$$

without internal extinction corrections, and

$$EW(\text{H}\alpha) = 28.8^{+7.2}_{-4.7} \text{ \AA} \quad (14)$$

after all corrections have been applied. The difference between these two values is due to the differential nature (line versus continuum) of the extinction law applied (Calzetti, Kinney & Storchi-Bergman 1994, Paper I).

The H α equivalent width is a measure of the rate of transformation of the ISM into stars, relative to the existing stellar population. Comparison of the dust-corrected equivalent width to the theoretical curves of Kennicutt *et al.* (1994) yields the birthrate parameter b , corresponding to the ratio of the star formation rate at the present time to that averaged over the age of the galactic disk. This interpretation is heavily dependent on the IMF used; for our adopted Salpeter (1955) IMF, we find

$$b = 0.26^{+0.10}_{-0.06} \quad (15)$$

which supports the common assertion that the cosmic star formation density has decreased substantially since $z \sim 1.5$ within star-forming galaxies. Other IMFs result in greater values of b , ranging as high as 2.8 for bottom-heavy IMFs such as Scalo (1986).

3.5. Gas cycling timescale

Using the SINGG data, we determine the gas cycling timescale t_{gas} , the time it would take for star formation to process the existing neutral and molecular ISM of a galaxy at its current rate of star formation. This value can be derived from H1 data if two assumptions are made. First, we assume that H1 emission occurs predominantly at low optical depth. Second, we assume that the ratio of molecular hydrogen to neutral atomic hydrogen remains constant, independent of the other characteristics of the galaxy.

To calculate t_{gas} we use the equation given in Paper I,

$$t_{\text{gas}} \approx 2.3 \left(\frac{\mathcal{M}_{\text{HI}}}{\text{SFR}} \right) \quad (16)$$

where $\mathcal{M}_{\text{gas}} = 2.3 \mathcal{M}_{\text{HI}}$, derived from the observations of Young *et al.* (1996), accounts for the typical molecular hydrogen as well as the helium content of the ISM.

The values of t_{gas} for our array of mass bins are given in Table 3. The volume-averaged gas cycling timescale for our sample can be derived from $t_{\text{gas}} \approx 2.3 (\rho_{\text{HI}}/\dot{\rho}_{\text{SFR}})$; with the values for ρ_{HI} and $\dot{\rho}_{\text{SFR}}$ presented in Section 3.1, we find this timescale to be $t_{\text{gas}} = 7.5^{+1.3}_{-2.1}$ Gyr. This is somewhat less than the Hubble time, consistent with the

previous findings of Kennicutt *et al.* (1994). Fig. 2 shows the gas cycling timescales for each of the SINGG galaxies, as well as the average within each H1 mass bin. While the galaxy-to-galaxy variation in t_{gas} is substantial (0.54 dex), the mean value does not appear to vary greatly with \mathcal{M}_{HI} .

Our choices of distance model and H1 Mass Function have much smaller impacts on the cosmic t_{gas} than they do on $\dot{\rho}_{\text{SFR}}$, and have no effect on the gas cycling times of the individual galaxies within our sample. Using the other H1 Mass Functions given in Table 2 result in cosmic t_{gas} values of 7.0 to 7.3 Gyr, well within the error bars of our adopted H1MF.

One should not take these gas cycling timescales too literally, as several of the assumptions behind them may be questioned. Much of the neutral interstellar medium may have a large optical depth, which would imply larger values of \mathcal{M}_{HI} than measured, causing t_{gas} to be somewhat underestimated. This effect probably results in a discrepancy of less than 20% (Haynes & Giovanelli 1984). As mentioned in Paper I, the observed ratio of ($\mathcal{M}_{\text{H2}}/\mathcal{M}_{\text{HI}}$) used to derive Eq. 16 has a dispersion of 0.58 dex, or almost a factor of 4; the ratio of CO luminosity to H $_2$ mass also has a large uncertainty. Hence, the t_{gas} estimate of any single galaxy is likely to be highly uncertain. Similarly, we have not accounted for systematic effects. It is well known that more massive and higher surface brightness galaxies are easier to detect in CO emission than dwarfs. In addition, our scenario does not include the “hot phase” of the ISM. This accounts for the X-ray emitting halos around galaxies as well as the intracluster medium and the intergalactic medium. This is likely to be the largest baryonic component of the universe (Fukugita, Hogan, & Peebles 1998). We also do not account for the return to the ISM of material processed by stars, the stellar yield. Because of these limitations we are careful not to imply that t_{gas} is a consumption timescale; rather, it is simply the time it would take for the present rate of star formation to form the mass of observed neutral ISM and inferred molecular ISM into new stars.

3.6. Dynamical parameters

The dynamical mass located within the optical radius of a galaxy, \mathcal{M}_{dyn} , is a useful way to estimate its mass (including both baryonic and dark matter) from easily observable quantities. The corresponding orbital time, t_{orb} , is also used for comparison with various models of galaxy evolution. To find these values, we first approximate the circular velocity of the edge of the galaxy from the FWHM spread in the velocities measured by H1PASS, corrected for the estimated inclination of each galaxy. That is,

$$v_{\text{circ}} = \left(\frac{W_{50}}{2 \sin(i)} \right). \quad (17)$$

where our inclination angle, i , is defined as

$$\sin^2(i) = \left(\frac{a^2 - b^2}{a^2 - c^2} \right) \quad (18)$$

(Bottinelli, Gouguenheim, Patural, & de Vaucouleurs 1983), where a, c are the axial lengths of the oblate spheroid fit to each galaxy, and a, b are the axial lengths

of the elliptical aperture used to measure optical fluxes. Since we do not wish to include any dependence on morphological classifications in the SINGG methodology, we assume a constant $(c/a) = 0.20$, except in three cases where our estimated (b/a) is less than this amount, where we simply set $c = b$. To reduce uncertainty in \mathcal{M}_{dyn} we exclude the 13 HI targets with multiple emission line galaxies, as well as 14 additional face-on galaxies ($(b/a) \geq 0.8$, or $i \leq 38^\circ$).

We then find the mass contained within the observed limit of each galaxy to be

$$\mathcal{M}_{\text{dyn}} = \left(\frac{v_{\text{circ}}^2 r_{\text{max}}}{G} \right) \quad (19)$$

and the orbital time to be

$$t_{\text{orb}} = \left(\frac{2\pi r_{\text{max}}}{v_{\text{circ}}} \right). \quad (20)$$

\mathcal{M}_{dyn} is evaluated using the radius at which we truncate our light profiles, r_{max} . This radius is found using only the optical light of the galaxy, therefore matter located outside it will not be included. \mathcal{M}_{dyn} is not a true total mass; rather, it is a crude estimate of the mass contained within the optical radius. Since HI typically extends beyond r_{max} with a flat rotation curve, the total mass (including dark matter) is larger, and our \mathcal{M}_{dyn} estimates are thus lower limits to the total mass. \mathcal{M}_{dyn} is compared with our HiPASS-derived values of \mathcal{M}_{HI} in Fig. 3a, and with our observed R band luminosity, L_R , in Fig. 3b. After excluding galaxies as explained above and fitting with a robust least absolute deviation fit, we find:

$$\log(\mathcal{M}_{\text{dyn}}) = 1.26 \log(\mathcal{M}_{\text{HI}}) - 1.36 \pm 0.37 \quad (21)$$

$$\log(\mathcal{M}_{\text{dyn}}) = 0.79 \log(L_R) + 2.83 \pm 0.36 \quad (22)$$

Eq. 21 implies that the fraction of \mathcal{M}_{dyn} made of HI is typically more than six times higher for our lowest HI masses ($\mathcal{M}_{\text{HI}} \approx 10^{7.5} M_\odot$) than it is for those at our high-mass extreme ($\mathcal{M}_{\text{HI}} \approx 10^{10.6} M_\odot$). Likewise, if we were to assume that \mathcal{M}/L remains constant over our range of dynamical masses, Eq. 22 would imply that the visible mass fraction is up to 10 times larger for our most massive galaxies as for our least massive. For any further equations requiring \mathcal{M}_{dyn} , we use the fit of Eq. 22 to set the dynamical mass of those galaxies excluded from our fit because of inclination or multiple H α sources. While Eq. 22 is reminiscent of the classic relations of Tully & Fisher (1977), our \mathcal{M}_{dyn} depends both on the width of the HI velocity profile and the optical radius, r_{max} . As a result, our result should not be directly compared to the Tully-Fisher relationship, $\mathcal{M}_* \sim v_{\text{circ}}^{3.1}$.

We are primarily interested in t_{orb} because it lets us address the redshift evolution of SFR in conjunction with the star formation law of Kennicutt (1998), which states that the global star formation law of galaxies is equivalent to galaxies converting 21% of their ISM mass within one orbital time t_{orb} evaluated at the radius where the HII region distribution is truncated, r_{HII} . We have not measured r_{HII} as such, for our sample. However, Paper I provides two radii that should bracket this: $r_{90}(\text{H}\alpha)$, the radius enclosing 90% of the H α flux, and r_{max} ; for most sources, r_{max} contains all the discernable emission in both R and H α . We evaluate the orbital time, t_{orb} ,

at these two radii. As with our determination of \mathcal{M}_{dyn} , t_{orb} is ill-determined for galaxies which have $i \leq 38^\circ$ or are in multiple ELG systems. In those cases we estimate $\log(t_{\text{orb}})$ from L_R using least absolute deviation fits, similar to Eq. 22:

$$\log(t_{\text{orb}}(r_{\text{max}})) = 0.099 \log(L_R) - 1.04 \pm 0.20 \quad (23)$$

$$\log(t_{\text{orb}}(r_{90}(\text{H}\alpha))) = 0.106 \log(L_R) - 1.35 \pm 0.23 \quad (24)$$

These fits are then used to set orbital times for the excluded galaxies, in the same manner as for \mathcal{M}_{dyn} .

As with HI mass, we use \mathcal{M}_{dyn} to find the local dynamical mass density, ρ_{dyn} , with Eq. 3. We find

$$\rho_{\text{dyn}} = 9.3^{+1.4}_{-1.6} \times 10^8 h_{70} M_\odot \text{ Mpc}^{-3}. \quad (25)$$

Again, we emphasize that this is only the mass density of the local universe residing within the optical radii of HI-rich galaxies. Of this density, 15% is found in galaxies with multiple H α sources, while an additional 34% is found in the face-on galaxies excluded from Eq. 22. Comparing to our HI mass density, ρ_{HI} , we estimate that 5.6% of the dynamical mass of local galaxies consists of neutral hydrogen in stars.

4. DISCUSSION

4.1. Completeness

One of our goals is to determine how representative an HI-selected sample is. To do this, we compare the R band luminosity density l'_R and dynamical mass density ρ_{dyn} derived from an HI-selected sample to those derived from more “complete” samples, such as the full SDSS sample set.

Our uncorrected value for l'_R , $4.4 \pm 0.7 \times 10^{37} h_{70} \text{ erg s}^{-1} \text{ \AA}^{-1} \text{ Mpc}^{-3}$, compares well to the SDSS-derived $^{0.1}r$ and $^{0.1}i$ band values of Blanton *et al.* (2003), 6.17 and $6.70 \times 10^{37} h_{70} \text{ erg s}^{-1} \text{ \AA}^{-1} \text{ Mpc}^{-3}$ respectively. Interpolating between these two bands by wavelength gives $l'_R \approx 6.30 \times 10^{37} h_{70} \text{ erg s}^{-1} \text{ \AA}^{-1} \text{ Mpc}^{-3}$ for the Sloan survey, which we will use as our “cosmic” R band density. Our estimated l'_R is approximately 70% of this value; therefore, the majority of the stars comprising the derived SDSS R band luminosity density are located in galaxies containing measurable quantities of HI. If we were to assume that our l'_R is low due to gas-poor galaxies (ellipticals) being absent from our sample, while our $l'_{\text{H}\alpha}$ is complete, then we can derive a corrected “cosmic” $EW(\text{H}\alpha) \approx l_{\text{H}\alpha}/(l_R/0.70) = 20.3^{+5.9}_{-3.5} \text{ \AA}$. This reduces the Salpeter-derived birthrate parameter to $b \approx 0.16^{+0.07}_{-0.03}$.

Note that the SR1 sample size implies that certain rare types of galaxies simply won’t be represented in these results. For instance, ultraluminous IR galaxies (ULIRGs, defined as $L_{\text{IR}} \geq 10^{12} L_\odot$, Sanders & Mirabel 1996) are rare enough that the volume contained within the HiPASS redshift and declination limits would only include roughly one ULIRG. As the sample used in this paper includes only 92 out of the 4315 HiPASS targets, it was extremely unlikely that any ULIRGs would be included in our observations.

When our dynamical mass density ρ_{dyn} is expressed as a fraction of the critical Einstein-de Sitter mass density ($\rho_{\text{crit}} = 1.36 \times 10^{11} h_{70}^2 M_\odot \text{ Mpc}^{-3}$), we find $\Omega_{\text{dyn}} = 0.0068 h_{70}^{-1}$, or 2.3% of Ω_0 in the concordance

cosmology. For comparison, Cole *et al.* (2001) estimates the $z \approx 0$ mass density of stars, Ω_{stars} , to be between 0.0029 (from an IR luminosity function) and 0.0020 (from star formation tracers). Similarly, the HI Mass Function of Zwaan *et al.* (2005) gives the local HI mass density to be $\approx 0.0004 h_{70}^{-1}$, which would imply a gas density on the order of $\Omega_{\text{gas}} = 0.0009 h_{70}^{-1}$ using the same logic as in Section 3.5. As a result, our ρ_{dyn} implies that around half of the mass located within the optical disks of nearby galaxies consists of gas and stars, with the remainder most likely consisting of dark matter.

This comparison must be viewed with some caution; our ρ_{dyn} is a crude estimate of all matter within the optical radii of HI-selected galaxies, including substantial quantities of dark matter. However, it excludes galactic gas (especially HI) extending beyond the optically-selected r_{max} , and also samples little of the hot plasma which resides in galaxy clusters and the intergalactic medium. We also do not sample any of the mass in HI-free galaxies, predominantly early-type galaxies. This comparison only shows that the mass we sample is comparable to the baryon content of the local star-forming galaxies, and that the ratio of baryonic matter to dark matter within these galaxies is substantially different than that of the universe as a whole.

4.2. $\dot{\rho}_{\text{SFR}}$ and $l_{\text{H}\alpha}$ in context

To compare our value of $\dot{\rho}_{\text{SFR}}$ to those found by other studies, we refer to Hopkins (2004), which compiled the results of 33 other star formation rate density papers and corrected each to a uniform Λ CDM cosmology, a Salpeter (1955) IMF, and with a Hubble constant of $H_0 = 70 \text{ km s}^{-1} \text{ Mpc}^{-1}$, $\Omega_0 = 0.3$, and $\Omega_\Lambda = 0.7$. We also include the IR-derived $\dot{\rho}_{\text{SFR}}(z)$ data of Pérez-González *et al.* (2005). The results before internal extinction correction are plotted in Fig. 4a, while the corrected values are plotted in Fig. 4b.

In Paper I we assert that SINGG is inherently less biased than other surveys, due to selecting sources by ISM content at radio wavelengths. Objective-prism surveys limit their samples by equivalent width and surface brightness, while an HI-selected sample can include diffuse sources or those with little star formation. If this is the case, we should expect to recover more star formation in the local universe. However, there are many steps involved in turning measured fluxes into luminosity density estimates; since techniques and assumptions vary between groups it is important to compare our results in as consistent a form as possible. Few previous studies present actual $\text{H}\alpha$ luminosity densities, and so our primary comparison will be between values of $\dot{\rho}'_{\text{SFR}}(z)$ corrected to our adopted IMF and extrapolated to $z = 0$. While some studies have only provided extinction-corrected $\dot{\rho}_{\text{SFR}}(z)$ estimates, in most cases we are able to work backwards using published corrections to derive $\dot{\rho}'_{\text{SFR}}(z)$ for each.

When the surveys located at $0.0 \leq z \leq 1.0$ are linearly fit to a simple $\dot{\rho}_{\text{SFR}}(z) = \dot{\rho}_{\text{SFR}}(0) (1+z)^\beta$ relationship, we find $\beta = 3.00 \pm 0.13$, which matches well with the $\beta = 3.2^{+0.7}_{-0.2}$ of Le Floch *et al.* (2005) and the $\beta = 3.1 \pm 0.5$ of Pérez-González *et al.* (2005). As a result, we will use this proportionality to extrapolate the star formation rate densities of low-redshift surveys to $z \sim 0$; the results

are given in Table 1.

The relative positions of the data points in Fig. 4a,b change due to the internal extinction correction. While the spread in points noticeably decreases between the two figures, we cannot claim to measure the highest corrected $\dot{\rho}_{\text{SFR}}(0)$. This is primarily due to our relatively mild extinction correction of 0.82 magnitudes, while the other samples noted in Table 1 have corrections ranging from 1.0 to 1.4 mag. Although mild, our correction correlates well with unpublished work from the 2dF Galaxy Redshift Survey (Folkes *et al.* 1999), which used the Balmer decrement to estimate the $\text{H}\alpha$ extinction of 160,000 line emitters; the typical value was found to be approximately 0.8 magnitudes. This discrepancy in $A_{\text{int}}(\text{H}\alpha)$ is most likely caused by the same luminosity bias mentioned above.

Even with a value of $\dot{\rho}_{\text{SFR}}$ comparable to other surveys, it is too early to declare a consensus because of the differences between the samples. For instance, we assert that the objective-prism selection method results in a large, consistent bias against non-starburst galaxies. Here we define starburst galaxies as those with $\text{H}\alpha$ equivalent widths within their half-light radii of $EW'_{50}(\text{H}\alpha) \geq 50 \text{ \AA}$, without correction for internal extinction. According to Heckman (1998), starbursts are estimated to comprise 15 – 20% of the population of the local universe. In the UCM spectroscopic survey, 72% of the sample consists of galaxies with equivalent widths above this threshold. For SINGG SR1, 16 out of the 110 $\text{H}\alpha$ sources (14.5%) met this criterion; these sources are collectively responsible for 25% of our final star formation rate density. If we assume that the HI-selected SINGG sample set is not significantly biased towards or against these galaxies, emission line-selected surveys (such as UCM) should be significantly underestimating the value of $\dot{\rho}_{\text{SFR}}$ due to underrepresentation of the non-starburst galaxies which appear to produce the majority of the star formation in the local universe.

4.3. Breakdown of luminosity density and $\dot{\rho}_{\text{SFR}}$

Fig. 5 shows the observed contributions to the R band and $\text{H}\alpha$ luminosity densities as a function of a variety of different quantities; this allows a comparison between our sample and other local samples of galaxies. Table 5 gives the values of each parameter at the 10th, 25th, 50th, 75th, and 90th percentiles of each luminosity density. In all cases, extinction and [NII] corrections have been applied as appropriate.

Plot (a) relates the luminosity densities to the HiPASS HI mass. We find that 72% of l_R and 70% of $l_{\text{H}\alpha}$ are found in galaxies with HI masses below our value of $\mathcal{M}_*(\text{HI})$. However, 77% of ρ_{HI} falls below this value, so the stellar luminosity density and $\dot{\rho}_{\text{SFR}}$ are slightly weighted towards higher HI masses than ρ_{HI} .

Plot (b) relates the luminosity densities to the dynamical mass, with the fit from Fig. 3b used to estimate dynamical masses for those galaxies with multiple sources or low axial ratios. Galaxies with low dynamical masses contribute substantially more to the $\text{H}\alpha$ luminosity than the R band density, and the SINGG sample extends across a wide range of \mathcal{M}_{dyn} values.

Plot (c) relates l to the R band luminosity by way of the absolute magnitude, M_R . As expected, galaxies with high R band luminosities contribute more to l_R than to

$l_{\text{H}\alpha}$. For comparison, the study of Brinchmann *et al.* (2004) used a stellar mass function with its knee at $\mathcal{M}_* = 10^{10.95} \mathcal{M}_\odot$; as this is a stellar mass (not simply H I mass), it should be approximately proportional to the R band luminosity. The 10th and 50th percentiles for $l_{\text{H}\alpha}$ in Brinchmann *et al.* (2004) were quoted as $\log(\mathcal{M}_*) = 9.0$ and 10.3, respectively, a difference of 1.3 dex. For comparison, the corresponding SINGG values of M_R for those percentiles differ by 4.1 magnitudes (1.7 dex), as shown in Table 5.

Plot (d) relates l to the star formation rate of each galaxy (directly proportional to $\text{H}\alpha$ luminosity, as shown in Eq. 4.) As expected, galaxies with high $\text{H}\alpha$ luminosities contribute more to $l_{\text{H}\alpha}$ than l_R . However, the fraction of $\text{H}\alpha$ luminosity density caused by luminous galaxies in SINGG is significantly lower than in other surveys. Only 12.2% of the SINGG $l_{\text{H}\alpha}$ is caused by galaxies with observed star formation rates greater than $10.0 \mathcal{M}_\odot \text{ yr}^{-1}$ once extinction corrections have been applied. For comparison, we integrate the luminosity functions quoted by other surveys; the UCM study of Gallego *et al.* (1995) has 26.5% of its $l_{\text{H}\alpha}$ come from galaxies above this threshold, while Tresse & Maddox (1998) has 23.1%. At the extreme cases, Sullivan *et al.* (2000) has only 9.3%, while Pérez-González *et al.* (2003) has 51.4% of its luminosity density come from galaxies with star formation rates above $10.0 \mathcal{M}_\odot \text{ yr}^{-1}$. This further illustrates that the apparent consensus in $\dot{\rho}_{\text{SFR}}$ may hide important differences in the various surveys of local star formation.

Plot (e) relates l to the narrow-band internal dust extinction correction, $A(\text{H}\alpha)$. While the extinction correction in our overall $\text{H}\alpha$ luminosity density is 0.82 magnitudes, only 37% of the R density comes from galaxies with smaller values, compared to 47% of the $\text{H}\alpha$ density. That is, l_R is weighted towards the more luminous galaxies, which have higher internal extinctions.

Plots (f) and (g) relate l to the effective (50% flux) radii found in the R and $\text{H}\alpha$ images, while plot (h) relates l to the ratio of these two radii. Again, these plots support the “downsizing” model of star formation; galaxies with large radii tend to contribute more to the R band luminosity density than the $\text{H}\alpha$ density, while galaxies with small radii contribute substantially more to $l_{\text{H}\alpha}$ than l_R . The luminosity density contributions are evenly distributed over our range of $(r_e(\text{H}\alpha)/r_e(R))$. Galaxies with centrally-located star formation ($r_e(\text{H}\alpha)/r_e(R) \leq 1.0$, suggestive of starbursts) do not dominate the luminosity densities; this contradicts what has been observed in other studies, such as the UCM survey of Gallego *et al.* (1995).

In all of the above plots, the smaller, less massive galaxies contribute substantially more to the SINGG $\text{H}\alpha$ luminosity density (and by extension, $\dot{\rho}_{\text{SFR}}$) than they do to the R band density. This reinforces the “downsizing” model, where star formation activity shifts to smaller galaxies over time (Cowie, Songaila, Hu, & Cohen 1996).

Plot (i) relates l to the ratio of the 90% flux radius to the half-light radius in the R band. The inverse of this ratio (referred to as the “concentration index”) has been examined by Shimasaku *et al.* (2001) using SDSS data. In that work, it was estimated that the boundary between bulge-dominated “early-type” and disk-dominated “late-type” galaxies occurred at a ratio

of $r_{90}(r')/r_e(r') = 3.03$. Given that definition, we estimate that 71% of our R density ($(3.2 \pm 0.5) \times 10^{37} h_{70} \text{ erg s}^{-1} \text{ \AA}^{-1} \text{ Mpc}^{-3}$ before extinction correction) and 82% of our $\text{H}\alpha$ density can be attributed to “late-type” galaxies, assuming the r -derived boundary does not change when shifted to our R band. For comparison, Hogg *et al.* (2002) find that 38% of the SDSS $^{0.1}i$ band luminosity density comes from “red-type” (assumed to be bulge-dominated early-type) galaxies, meaning that a total of $4.1 \times 10^{37} h_{70} \text{ erg s}^{-1} \text{ \AA}^{-1} \text{ Mpc}^{-3}$ can be attributed to late-type galaxies. As their definition of red galaxies was conservative, this percentage should include some early-type galaxies. Likewise, Baldry *et al.* (2004) fit a bimodal distribution to observed galaxy colors to determine that 58% of the SDSS $^{0.1}r$ band luminosity density comes from blue galaxies (for a density of $3.6 \times 10^{37} h_{70} \text{ erg s}^{-1} \text{ \AA}^{-1} \text{ Mpc}^{-3}$). As a result, while the SINGG survey recovers around 70% of the SDSS l_R , we recover a larger fraction (80 – 90%) of the luminosity density from late-type galaxies.

Plot (j) shows the dependence of l on $\text{H}\alpha$ equivalent width. The $\dot{\rho}_{\text{SFR}}$ derived from the UCM spectroscopic survey (Gallego *et al.* 1995) uses only galaxies with equivalent widths larger than 10 \AA . According to our data, 24.1% of the local extinction-corrected R band luminosity density and 4.5% of the corrected $\text{H}\alpha$ luminosity density come from galaxies with equivalent widths below this threshold.

Plots (k) and (l) relate l to surface brightnesses, $\mu_e(R)$ and $\Sigma_e(\text{H}\alpha)$. As expected, galaxies with high $\text{H}\alpha$ surface brightnesses (i.e., starbursts) contribute a much larger fraction of $l_{\text{H}\alpha}$ than of l_R . For comparison, the SDSS-derived sample of Blanton *et al.* (2005) has a surface brightness limit of $\mu_e(R) = 24.0 \text{ ABmag arcsec}^{-2}$; 1.1% of our l_R and 1.2% of $l_{\text{H}\alpha}$ come from galaxies below this cutoff.

4.4. Recent redshift evolution in $\dot{\rho}_{\text{SFR}}(z)$

Fig. 4b shows that the $\dot{\rho}_{\text{SFR}}(z)$ has declined by approximately a factor of ten from $z \sim 1$ to the present. Specifically, fitting the internal dust corrected data with $z \leq 1$ with a robust (outlier resistant) linear fit

$$\log(\dot{\rho}_{\text{SFR}}(z)) = \log(\dot{\rho}_{\text{SFR}}) + \eta z \quad (26)$$

yields $\log(\dot{\rho}_{\text{SFR}} [\mathcal{M}_\odot \text{ yr}^{-1} \text{ Mpc}^{-3}]) = -1.73$ and $\eta = 1.02$ dex per redshift. We can estimate the systematic uncertainties in this fit by categorizing the $\dot{\rho}_{\text{SFR}}(z)$ data by the star formation tracer used in each measurement: (1) optical emission lines; (2) ultraviolet continuum; and (3) FIR or radio continuum. This yields $\log(\dot{\rho}_{\text{SFR}}) = -1.80, -1.53, -1.94$, and $\eta = 1.05, 0.43, 1.37$ for survey types 1, 2, and 3, respectively. This suggests that the uncertainties in the zeropoint and slope are 0.20 and 0.47 dex, respectively.

What causes the decrease in $\dot{\rho}_{\text{SFR}}(z)$ with cosmic time? Recently, Kauffmann *et al.* (2004) presented a model of the recent star formation history of galaxies in the local universe that provides a useful context to answering this question. In their model, star formation events occur when galaxies merge; subsequently, the SFR inside the galaxy decays according to a prescription similar in nature to the star formation laws of Kennicutt (1998) and Dopita & Ryder (2005). They use a high-resolution Cold

Dark Matter (CDM) simulation, identify galaxy mergers with CDM halo mergers, and parameterize the form of their star formation law by the average stellar mass density. Essentially, the physics of their model can be separated into CDM effects (the merger of halos), and baryonic physics (the star formation law). We can then rephrase the question above: is the decrease in $\dot{\rho}_{\text{SFR}}(z)$ with cosmic time driven by CDM or baryonic physics? Are we seeing a recent decrease in the merger rate of halos? Or, are we seeing the secular decay of the SFR after a much earlier decrease in the halo merger rate?

The dynamical information on our sample provided by the H I line widths provides a means to address this question. The orbital time, t_{orb} , has been evaluated at two radii, $r_{90}(\text{H}\alpha)$ and r_{max} , as explained in Section 3.6. Using the same methods as those in Section 4.3, we find that the 25%, median, and 75% contributions to $l_{\text{H}\alpha}$ (and, by extension, $\dot{\rho}_{\text{SFR}}$) in our sample occur for $t_{\text{orb}} = 0.30, 0.57, 0.60$ Gyr when evaluated at $r_{90}(\text{H}\alpha)$ and $0.56, 1.00, 1.03$ when evaluated at r_{max} .

We can use the orbital times to estimate the change in SFR with redshift for the galaxies in our sample obeying Eq. 26. If we assume that the star formation law remains invariant over this timescale, then consumption of 21% of the ISM is equivalent to a 21% decrease in the SFR over t_{orb} (Kennicutt 1998). Translating t_{orb} to a look back time, the logarithmic change in SFR is given by

$$\frac{\delta \log(\text{SFR}[\mathcal{M}_{\odot} \text{ yr}^{-1}])}{\delta z} \approx \frac{1.43 h_{70}}{t_{\text{orb}} [\text{Gyr}]} \quad (27)$$

in the same units as the slope η in Eq. 26. The median t_{orb} translates to $\delta \log(\text{SFR})/\delta z = 2.5, 1.4$ as defined by $r_{90}(\text{H}\alpha)$ and r_{max} , while the interquartile ranges are $4.8 - 2.4$ and $2.6 - 1.4$, respectively. We see that the SFR of the galaxies in our sample will decay over a wide range of timescales. However, a galaxy with t_{orb} similar to the median galaxy in our sample will have its star formation decay at a rate similar to that observed in the universe as a whole.

5. CONCLUSIONS

Our measurement of the local star formation rate density, $\log(\dot{\rho}_{\text{SFR}} [\mathcal{M}_{\odot} \text{ yr}^{-1} \text{ Mpc}^{-3}]) = -1.80 + \log(h_{70})$, is similar to those of most previous $z \sim 0$ studies, as shown in Table 1. When compared to the results of other sur-

veys, this agrees with the consensus that the star formation rate density has decreased by an order of magnitude from a redshift of $z \sim 1$ to the present. While a consensus in $\dot{\rho}_{\text{SFR}}$ appears to be emerging, this may be largely illusory. There remain significant differences between the various surveys in terms of extinction corrections and the contributions of various types of galaxies to the totals. Systematic effects are large and need to be accounted for before a true consensus can emerge.

The decreasing $\dot{\rho}_{\text{SFR}}(z)$ with cosmic time has important implications for models of galaxy evolution, as this trend suggests a shift from the faster “burst” star formation process to the slower “quiescent” process, with the greater fraction of the total star formation occurring in non-starburst galaxies. This is supported by the results presented in Section 4.4, which suggest that the decrease in $\dot{\rho}_{\text{SFR}}(z)$ with cosmic time is largely driven by the secular decay in SFR after earlier accretion events. That is, the current evolution in $\dot{\rho}_{\text{SFR}}(z)$ is largely driven by interior baryon physics rather than the merger of CDM dominated halos. This interpretation is consistent with the relatively small fraction of multiple ELG systems and targets that look like recent mergers (15 out of 93 HiPASS pointings included in SR1, see Paper I), as well as the work of Bell *et al.* (2005). In contrast, at $z > 1$ field galaxies tend to have a disturbed morphology suggesting a higher fraction of interacting and merging systems and very few regular disk galaxies can be discerned. It is tempting to speculate that $z \sim 1$ represents the epoch where cosmic evolution transitions from being driven largely by CDM interactions to being driven by the internal self-regulation of star formation.

Partial financial support for this work has been provided by NASA grant NAG5-13083 (LTSA program) to G.R. Meurer, as well as the Director’s Discretionary Research Fund of the Space Telescope Science Institute. We would like to thank the many people whose feedback helped in the development of this paper, including Jesús Gallego, Pablo Pérez-González, Joe Helmboldt, and Jarle Brinchmann. We would also like to thank the National Optical Astronomy Observatory (NOAO) for their support, especially the staff of the Cerro Tololo Inter-American Observatory.

REFERENCES

- Baldry, I.K., Glazebrook, K., Brinkmann, J., Ivezić, Ž., Lupton, R.H., Nichol, R.C., & Szalay, A.S. 2004, ApJ, 600, 681
 Barnes, D.G., *et al.* 2001, MNRAS, 322, 486
 Bell, E.F. 2003, ApJ, 586, 794
 Bell, E.F., *et al.* 2005, ApJ, 625, 23
 Blanton, M.R., *et al.* 2003, ApJ, 592, 819
 Blanton, M.R., Lupton, R.H., Schlegel, D.J., Strauss, M.A., Brinkmann, J., Fukugita, M., & Loveday, J. 2005, ApJ, 631, 208
 Bottinelli, L., Gougouenheim, L., Paturel, G., & de Vaucouleurs, G. 1983, A&A, 118, 4
 Brinchmann, J., Charlot, S., White, S.D.M., Tremonti, C., Kauffmann, G., Heckman, T., & Brinkmann, J. 2004, MNRAS, 351, 1151
 Calzetti, D., Kinney, A.L., & Storchi-Bergmann, T. 1994, ApJ, 429, 582
 Cole, S., *et al.* 2001, MNRAS, 326, 255
 Cowie, L.L., Songaila, A., Hu, E.M., & Cohen, J.G. 1996, AJ, 112, 839
 Devereux, N.A. & Eales, S.A. 1989, ApJ, 340, 708
 Dopita, M.A. & Ryder, S.D. 1994, ApJ, 430, 163
 Fanelli, M.N., O’Connell, R.W., & Thuan, T.X. 1988, ApJ, 334, 665
 Flores, H., Hammer, F., Thuan, T.X., Césarsky, C., Desert, F.X., Omont, A., Lilly, S.J., Eales, S., Crampton, D., & Le Fèvre, O. 1999, ApJ, 517, 148
 Folkes, S., *et al.* 1999, MNRAS, 308, 459
 Fukugita, M., Hogan, C.J., & Peebles, P.J.E. 1998, ApJ, 503, 518
 Gallego, J., Zamorano, J., Aragón-Salamanca, A., & Rego, M. 1995, ApJ, 455, L1
 Gronwall, C., 1997, AAS, 191.7602G
 Haynes, M.P. & Giovanelli, R. 1984, AJ, 89, 758
 Heckman, T. 1998, in “Origins”, ASP Conference Series, 148, 127
 Helmboldt, J.F., Walterbos, R.A.M., Bothun, G.D., O’Neil, K., & de Blok, W.J.G. 2004, ApJ, 613, 914
 Hogg, D.W. *et al.* 2002, AJ, 124, 646
 Hopkins, A.M. 2004, ApJ, 615, 209
 Jansen, R.A. 2000, Ph.D. thesis, Kapteyn Astronomical Institute
 Karachentsev, I.D., Karachentseva, V.E., Huchtmeier, W.K., & Markov, D.I. 2004, AJ, 127, 2031

- Kauffmann, G., White, S.D.M., Heckman, T.M., Ménard, B., Brinchmann, J., Charlot, S., Tremonti, C., & Brinkmann, J. MNRAS, 353, 713
- Kennicutt, R.C., Tamblyn, P., & Congdon, C.E 1994, ApJ, 435, 22
- Kennicutt, R.C., Jr. 1998, ApJ, 498, 541
- Koribalski, B.S. *et al.* 2004, AJ, 128, 16
- Kroupa, P. 2001, MNRAS, 322, 231
- Le Floch, E., *et al.* 2005, ApJ, 632, 169
- Madau, P., Ferguson, H.C., Dickinson, M.E., Giavalisco, M., Steidel, C.C., & Fruchter, A. 1996, MNRAS, 283, 1388
- Madau, P., Pozzetti, L., & Dickinson, M. 1998, ApJ, 498, 106
- Meurer, G.R., *et al.* 2006, ApJ, accepted (astro-ph/0604444)
- Meyer, M.J., *et al.* 2004, MNRAS, 350, 1195
- Mould, J.R., *et al.* 2000, ApJ, 528, 655
- Pei, Y.C. & Fall, S.M. 1995, ApJ, 454, 69
- Pei, Y.C., Fall, S.M., & Hauser, M.G. 1999, ApJ, 522, 604
- Pérez-González, P.G., Zamorano, J., Gallego, J., Aragón-Salamanca, A., & de Paz, A.G. 2003, ApJ, 591, 827
- Pérez-González, P.G., *et al.* 2005, ApJ, 630, 82
- Putman, M.E., *et al.* 2002, AJ, 123, 873
- Roberts, M.S. 1962, AJ, 67, 437
- Rosenberg, J.L., & Schneider, S.E. 2002, ApJ, 567, 247
- Salpeter, E. 1955, ApJ, 121, 161
- Salzer, J. 1989, ApJ, 347, 152
- Sanders, D.B. & Mirabel, I.F. 1996, ARAA, 34, 749
- Scalo, J.M. 1986, Fundamentals of Cosmic Physics, 11, 1
- Schlegel, D.J., Finkbeiner, D.P., & Davis, M. 1998, ApJ, 500, 525
- Serjeant, S., Gruppioni, C., & Oliver, S. 2002, MNRAS, 330, 621
- Shimasaku, K. *et al.* 2001, AJ, 122, 1238
- Somerville, R.S., Primack, J.R., & Faber, S.M. 2001, MNRAS, 320, 504
- Staveley-Smith, L. *et al.* 1996, PASAu, 13, 243
- Sullivan, M., Treyer, M.A., Ellis, R.S., Bridges, T.J., Milliard, B., & Donas, J. 2000, MNRAS, 312, 442
- Tremonti, C.A., Heckman, T.M., Kauffmann, G., Brinchmann, J., Charlot, S., White, S.D.M., Seibert, M., Peng, E.W., Schlegel, D.J., Uomoto, A., Fukugita, M., & Brinkmann, J. 2004, ApJ, 613, 898
- Tresse, L. & Maddox, S.J. 1998, ApJ, 495, 691
- Treyer, M.A., Ellis, R.S., Milliard, B., Donas, J. & Bridges, T.J. 1998, MNRAS, 300, 303
- Tully, R.B., & Fisher, J.R. 1977, AA, 54, 661
- Young, J.S., Allen, L., Kenney, D.P., Lesser, A., & Rownd, B. 1996, AJ, 112, 1903
- Yun, M.S., Reddy, N.A., & Condon, J.J. 2001, ApJ, 554, 803
- Zwaan, M.A., *et al.* 2003, AJ, 125, 2842
- Zwaan, M.A., *et al.* 2004, MNRAS, 350, 1210
- Zwaan, M.A., Meyer, M.J., Staveley-Smith, L., & Webster, R.L. 2005, MNRAS, 359, L30

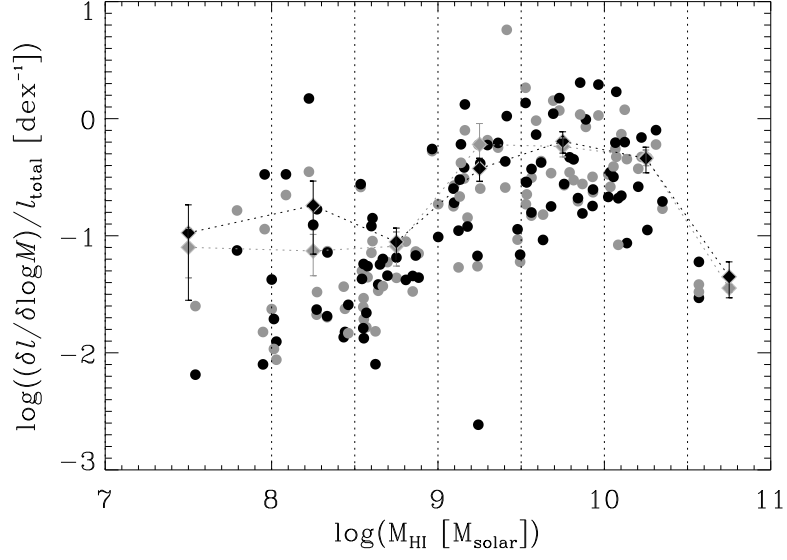


FIG. 1.— Fraction of total luminosity density per H I mass decade. Dark symbols represent H α , while lighter symbols denote R band luminosities. Circles represent the value for the individual SINGG galaxies. Diamonds and error bars are the average values and standard deviations of mean for each mass bin. All values are corrected for internal extinction.

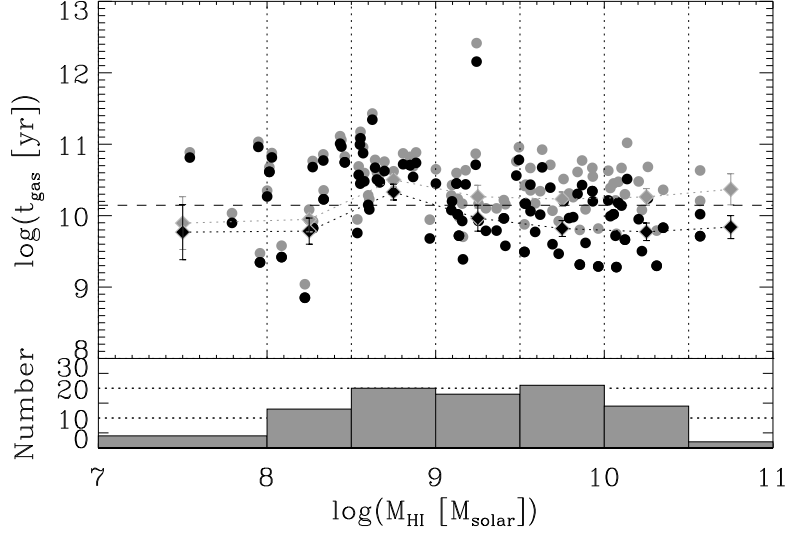


FIG. 2.— Gas cycling timescale and histogram. Circles are values for individual galaxies. Diamonds and error bars are the average values and standard deviations of mean for each mass bin. The dashed line corresponds to the Hubble time (13.6 Gyr). Dark symbols are corrected for internal extinction, lighter symbols are uncorrected values for the same galaxies.

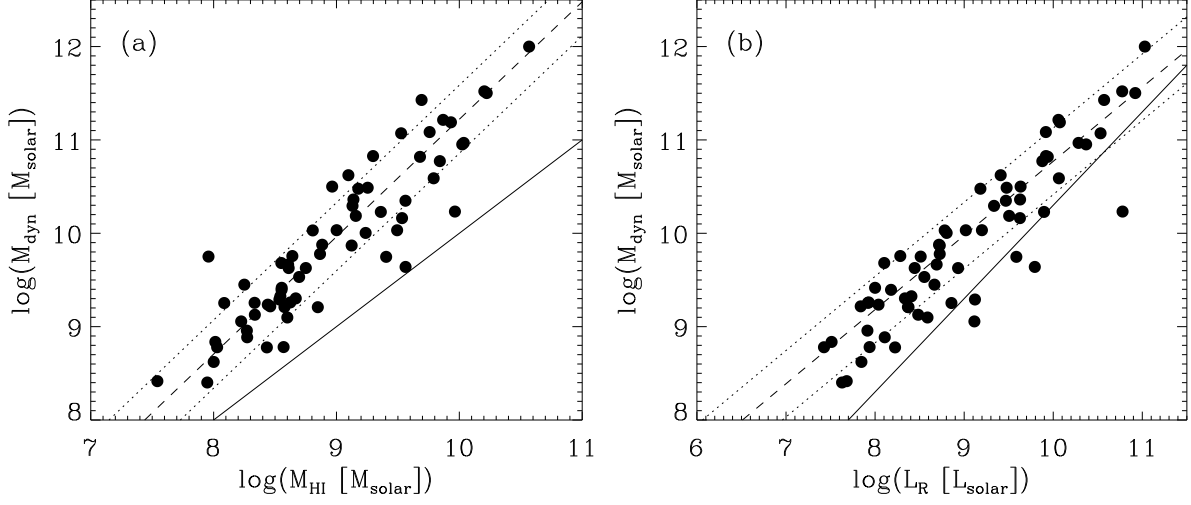


FIG. 3.— Dynamical mass as a function of (a) HI mass and (b) R band luminosity. The dashed lines show the best fits, with dotted lines showing the dispersion for each. Solid lines show (a) $M_{\text{dyn}} = M_{\text{HI}}$ and (b) $M_{\text{dyn}} = 2 L_{\text{R}}$ in solar units (where $M/L_{\text{R}} \approx 2$ is typical of gas-rich galaxies).

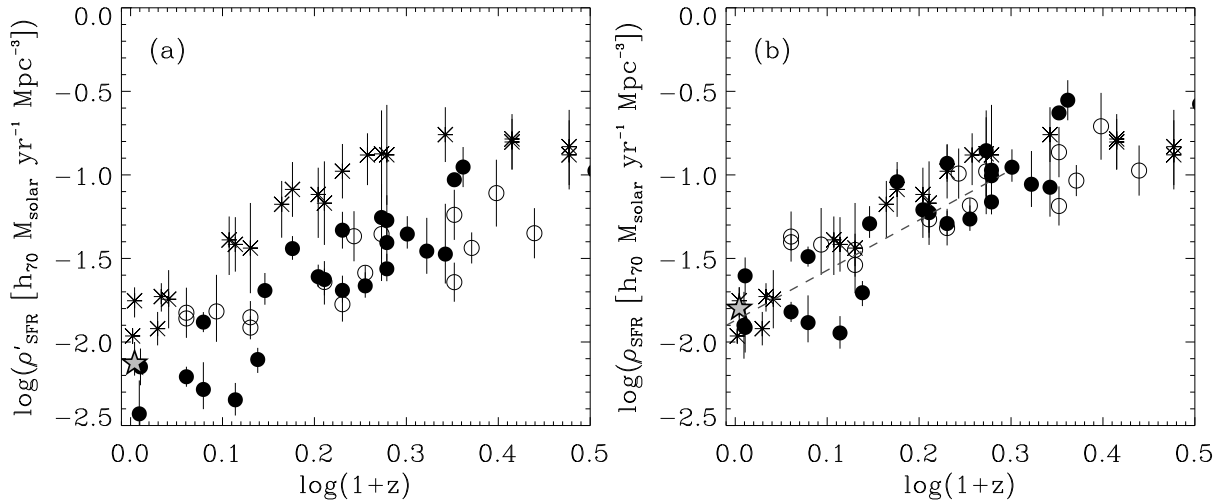


FIG. 4.— Star formation rate density, (a) without and (b) with corrections made for internal dust extinction. Solid circles are emission-line surveys (usually $\text{H}\alpha$). Hollow circles are UV surveys. Asterisks are IR/sub-mm surveys. The star at $z \approx 0$ is the SINGG value. Other values are drawn from Hopkins (2004) and Pérez-González *et al.* (2005). The dashed line in (b) corresponds to the best fit from $0 < z < 1$.

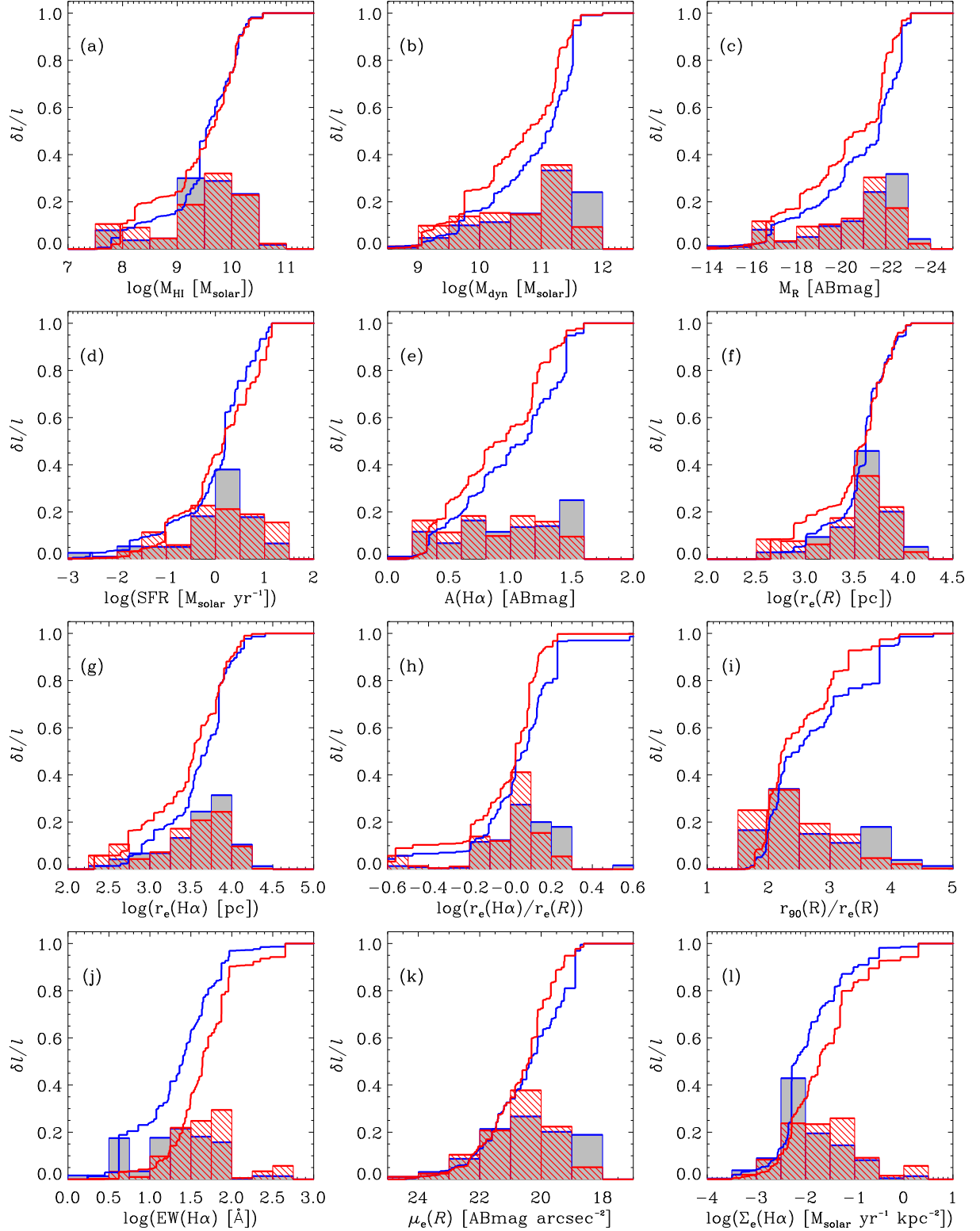


FIG. 5.— Fraction of the total luminosity density, l , as a function of various quantities. Red lines correspond to $H\alpha$ luminosity, while blue lines correspond to R band luminosity. Cumulative values as well as binned histograms are given for each.

TABLE 1
LOCAL H α COSMIC STAR FORMATION RATE DENSITY MEASUREMENTS

Survey	Sources	z	$\log(\dot{\rho}'_{\text{SFR}}(z))$	$\log(\dot{\rho}_{\text{SFR}}(z))$	$\log(\dot{\rho}'_{\text{SFR}}(0))$	$\log(\dot{\rho}_{\text{SFR}}(0))$
SINGG	110	0.01	$-2.13^{+0.08}_{-0.09}$	$-1.80^{+0.13}_{-0.08}$	$-2.14^{+0.08}_{-0.09}$	$-1.81^{+0.13}_{-0.08}$
UCM (1)	264	0.02	-2.45 ± 0.20	-1.92 ± 0.20	-2.48 ± 0.20	-1.95 ± 0.20
UCM (2)	79	0.03	-2.15 ± 0.11	-1.60 ± 0.11	-2.19 ± 0.11	-1.64 ± 0.11
SDSS (3)	149660	0.10	...	-1.54 ± 0.07	...	-1.66 ± 0.07
FOCA (4)	216	0.15	-2.21 ± 0.15	-1.82 ± 0.06	-2.39 ± 0.15	-2.00 ± 0.06
CFRS (5)	110	0.20	-1.88 ± 0.06	-1.49 ± 0.06	-2.12 ± 0.06	-1.73 ± 0.06

NOTE. — Units for columns 4-7 are [$\mathcal{M}_{\odot} \text{ yr}^{-1} \text{ Mpc}^{-3}$]; $\dot{\rho}'_{\text{SFR}}(z)$ and $\dot{\rho}_{\text{SFR}}(z)$ are the SFR density estimates without and with internal dust extinction corrections, respectively, evaluated at the mean redshift z of the survey. The corresponding $z = 0$ rates are extrapolated assuming $\dot{\rho}_{\text{SFR}}(z) = \dot{\rho}_{\text{SFR}}(0) (1+z)^3$

- 1: Gallego *et al.* (1995)
 2: Pérez-González *et al.* (2003)
 3: Brinchmann *et al.* (2004)
 4: Sullivan *et al.* (2000)
 5: Tresse & Maddox (1998)

TABLE 2
HI MASS FUNCTIONS

HiMF (1)	α (2)	$\log(\mathcal{M}_{\star})$ (3)	$\theta_{\star} \times 10^3$ (4)	$\log(\dot{\rho}_{\text{SFR}})$ (5)	$\log(\rho_{\text{HI}})$ (6)
This paper	-1.41 ± 0.05	9.92 ± 0.04	3.9 ± 0.7	$-1.80^{+0.13}_{-0.08}$	7.71 ± 0.03
Zwaan <i>et al.</i> (2005)	-1.37 ± 0.03	9.86 ± 0.03	4.9 ± 0.7	$-1.77^{+0.15}_{-0.11}$	$7.73^{+0.06}_{-0.08}$
Zwaan <i>et al.</i> (2003)	-1.30 ± 0.08	9.85 ± 0.06	7.5 ± 1.7	$-1.62^{+0.13}_{-0.08}$	7.88 ± 0.02
Rosenberg & Schneider (2002)	-1.53	9.94	4.72	$-1.58^{+0.14}_{-0.10}$	7.91 ± 0.01

NOTE. — Column descriptions [units]: (1) Source reference. (2) Schechter fit power-law constant. (3) Schechter fit characteristic HI mass [\mathcal{M}_{\odot}]. (4) Schechter fit normalization [$\text{Mpc}^{-3} \text{ dex}^{-1}$]. (5) Star formation rate density [$\mathcal{M}_{\odot} \text{ yr}^{-1} \text{ Mpc}^{-3}$]. (6) HI mass density [$\mathcal{M}_{\odot} \text{ Mpc}^{-3}$].

TABLE 3
COSMIC STAR FORMATION AS A FUNCTION OF MASS

$\log(\mathcal{M}_{\text{HI}}/\mathcal{M}_{\odot})$ (1)	N (2)	t_{gas} (3)	$\dot{\rho}_{\text{SFR}}$ per $\log(\mathcal{M}_{\text{HI}}/\mathcal{M}_{\odot})$ (4)	l_R per $\log(\mathcal{M}_{\text{HI}}/\mathcal{M}_{\odot})$ (5)
7.0 – 8.0	4	5.9 ± 0.5	$(1.68 \pm 1.31) \times 10^{-3}$	$(5.53 \pm 3.06) \times 10^{36}$
8.0 – 8.5	13	6.1 ± 0.4	$(2.88 \pm 3.23) \times 10^{-3}$	$(5.15 \pm 2.69) \times 10^{36}$
8.5 – 9.0	20	21.4 ± 3.1	$(1.41 \pm 0.61) \times 10^{-3}$	$(5.66 \pm 2.52) \times 10^{36}$
9.0 – 9.5	18	9.2 ± 2.3	$(5.96 \pm 1.38) \times 10^{-3}$	$(41.9 \pm 33.1) \times 10^{36}$
9.5 – 10.0	21	6.6 ± 1.1	$(10.2 \pm 2.3) \times 10^{-3}$	$(40.2 \pm 8.2) \times 10^{36}$
10.0 – 10.5	14	5.9 ± 1.0	$(7.28 \pm 1.98) \times 10^{-3}$	$(32.5 \pm 5.2) \times 10^{36}$
10.5 – 11.0	2	6.9 ± 0.7	$(0.71 \pm 0.17) \times 10^{-3}$	$(2.48 \pm 0.13) \times 10^{36}$

NOTE. — Column descriptions [units]: (1) HI mass range. (2) Number of galaxies within HI mass range. (3) Gas cycling timescale [Gyr]. (4) Star formation rate density contribution per decade of HI mass [$\mathcal{M}_{\odot} \text{ yr}^{-1} \text{ Mpc}^{-3} \text{ dex}^{-1}$]. (5) R band luminosity density contribution per decade of HI mass [$\text{erg s}^{-1} \text{ \AA}^{-1} \text{ Mpc}^{-3} \text{ dex}^{-1}$].

TABLE 4
ERROR BUDGET FOR LUMINOSITY DENSITIES

Uncertainty	Uncertainty in log(luminosity density)			
	l'_R	l_R	$l'_{H\alpha}$	$l_{H\alpha}$
<i>Random Errors</i>				
H I mass function	± 0.029	± 0.027	± 0.034	± 0.029
Sampling	± 0.062	± 0.073	± 0.071	± 0.061
Sky subtraction	± 0.001	± 0.001	± 0.002	± 0.002
Continuum subtraction	± 0.010	± 0.015
Flux calibration	± 0.008	± 0.008	± 0.013	± 0.012
N II correction	$+0.004$ -0.006	$+0.005$ -0.008
Internal dust extinction	...	$+0.053$ -0.013	...	$+0.107$ -0.016
Total Random	± 0.069	$+0.094$ -0.080	$+0.078$ -0.083	$+0.127$ -0.075
<i>Systematic Errors</i>				
N II zeropoint	± 0.002	± 0.002
Internal dust zeropoint	...	± 0.003	...	± 0.006
Distance model	± 0.014	± 0.017	± 0.028	± 0.033
Total Systematic	± 0.014	± 0.017	± 0.028	± 0.033

TABLE 5
BREAKDOWN OF $l_{H\alpha}$ AND l_R BY GALAXY PARAMETERS

Percentile	10% ($R/H\alpha$)	25% ($R/H\alpha$)	50% ($R/H\alpha$)	75% ($R/H\alpha$)	90% ($R/H\alpha$)
$\log(\mathcal{M}_{HI} [\mathcal{M}_\odot])$	8.19/7.96	9.25/9.08	9.52/9.58	9.97/9.97	10.13/10.12
$\log(\mathcal{M}_{dyn} [\mathcal{M}_\odot])$	9.55/9.27	10.34/9.87	11.07/10.67	11.42/11.16	11.45/11.42
M_R [ABmag]	-16.86/-16.63	-19.64/-18.40	-21.68/-20.77	-22.49/-21.84	-22.69/-22.42
$\log(\text{SFR} [\mathcal{M}_\odot \text{ yr}^{-1}])$	-1.19/-1.05	-0.27/-0.33	0.19/0.17	0.45/0.74	0.89/1.04
$A(H\alpha)$ [ABmag]	0.34/0.32	0.66/0.51	1.11/0.92	1.38/1.18	1.45/1.36
$\log(r_e(R) [\text{pc}])$	3.01/2.88	3.47/3.37	3.61/3.61	3.73/3.73	3.89/3.88
$\log(r_e(H\alpha) [\text{pc}])$	2.90/2.73	3.42/3.17	3.69/3.54	3.84/3.83	4.07/3.99
$\log(r_e(H\alpha)/r_e(R))$	-0.19/-0.49	-0.06/-0.11	0.06/0.02	0.14/0.09	0.22/0.14
$r_{90}(R)/r_e(R)$	1.96/1.89	2.06/1.99	2.47/2.23	3.26/2.91	3.74/3.29
$\log(EW_{50}(H\alpha) [\text{\AA}])$	0.53/1.22	1.05/1.43	1.40/1.64	1.64/1.87	1.87/1.97
$\mu_e(R) [^\dagger]$	22.26/22.28	21.42/21.44	20.35/20.43	19.35/19.97	19.04/19.33
$\log(\Sigma_e(H\alpha) [^\ddagger])$	-2.57/-2.55	-2.31/-2.28	-2.19/-1.72	-1.58/-1.28	-1.02/-0.68

NOTE. —

† : units are [ABmag arcsec $^{-2}$]

‡ : units are [$\mathcal{M}_\odot \text{ yr}^{-1} \text{ kpc}^{-2}$]